Nat. Hazards Earth Syst. Sci. Discuss., 3, 5633–5664, 2015
www.nat-hazards-earth-syst-sci-discuss.net/3/5633/2015/
doi:10.5194/nhessd-3-5633-2015

Natural Hazards and Earth System Sciences
Discussions
Open Access

Automated object-based classification of rain-induced landslides with VHR multispectral images in Madeira Island

S. Heleno, M. Matias, P. Pina, and A. J. Sousa

CERENA, Instituto Superior Técnico, University of Lisbon, Lisbon, Portugal

Received: 30 July 2015 – Accepted: 27 August 2015 – Published: 23 September 2015

Correspondence to: S. Heleno (sandra.heleno@ist.utl.pt)

Published by Copernicus Publications on behalf of the European Geosciences Union.

Abstract

A method for semi-automatic landslide detection, with the ability to separate source and run-out areas, is presented in this paper. It combines object-based image analysis and a Support Vector Machine classifier on a GeoEye-1 multispectral image, sensed 3 days after the major damaging landslide event that occurred in Madeira island (20 February 2010), with a pre-event LIDAR Digital Elevation Model. The testing is developed in a 15 km^2-wide study area, where 95 % of the landslides scars are detected by this supervised approach. The classifier presents a good performance in the delineation of the overall landslide area. In addition, fair results are achieved in the separation of the source from the run-out landslide areas, although in less illuminated slopes this discrimination is less effective than in sunnier east facing-slopes.

1 Introduction

Landslides are complex mass movements that occur on hill slopes due to the action of gravity; they play an important role in the evolution of landforms, while constituting a serious natural hazard in many regions throughout the world. Landslides can involve flowing, sliding, toppling, or falling and are commonly associated with a trigger, with slope failures generally occurring within minutes after an earthquake, hours to days after a snowmelt, and days to weeks after an intense rainfall (Guzzetti et al., 2012; Malamud et al., 2004). Urban expansion into hilly or mountainous regions results in more people being exposed to the hazard, thus increasing landslide risks. Nowadays, landslides claim thousands of lives every year and result in extensive infrastructure and property damages (Holbling et al., 2012; Malamud et al., 2004; Yang and Chen, 2010). Landslide susceptibility, hazard, and risk assessment are important tools in land-use planning in order to avoid the urban expansion of vulnerable areas, thus reducing future economic and human losses. One of the best indicators for future landslide activity is evidence of past landslide activity: so for landslide hazard assessment, mapping landslides is an essential step (Aksoy et al., 2012; Bucknam et al., 2001; Lahousse et al., 2011; Guzzetti et al., 2012).

An inventory map records the location and, when known, the date of occurrence and types of landslides that have left discernible traces in an area (Malamud et al., 2004). A landslide-event inventory, consisting of all the slope failures associated with a single trigger such as an earthquake, rainstorm or snowmelt, is useful to determine the conditions of residual risk in the aftermath of the event, as a guide for emergency and recovery efforts, and to validate landslide susceptibility and hazard models (Guzzetti et al., 2012; Mondini et al., 2013, 2014; Malamud et al., 2004; Barlow et al., 2006). Immediately after a landslide event, individual landslides are usually clearly recognizable, even in the case of small, shallow landslides, such as soil slips or debris flows. Hence an inventory of e.g. rainfall-induced landslides can be significantly complete (i.e. include a substantial fraction of all landslides at all scales) if detailed mapping has been carried out shortly after the landslide event (Malamud et al., 2004). Despite this, landslide inventories are generally incomplete, both with respect to the area covered and to the time period investigated, which is a serious drawback for landslide hazard studies (Malamud et al., 2004; van Westen et al., 2006).

Landslide inventories are traditionally derived by visual interpretation of aerial photographs and field surveys. Field surveys can obtain comprehensive and precise landslide inventories, but they are very limited in terms of cost-effectiveness and logistical constraints, particularly over large or limited access areas (Yang and Chen, 2010). Interpretation of stereoscopic aerial photography (where the interpreter detects and classifies landslides based on experience and on the analysis of changes in the form, shape, position, or appearance of the topographic surface) remains the most common method to recognize landslides, despite being an empirical and subjective technique (Guzzetti et al., 2012). Aerial photographs can accurately depict the distribution and contours of landslides in a region, but they are usually not available in a timely manner, restricting the ability to prepare event and seasonal inventory maps repeatedly and for large areas (Aksoy et al., 2012; Martha et al., 2010; Guzzetti et al., 2012). In this context satellite imagery emerges as a uniquely reliable tool for immediate mapping of landslides and damage assessment over large and inaccessible areas (Holbling et al., 2012; Aksoy et al., 2012; Joyce et al., 2008; Barlow et al., 2006; Xu et al., 2015). Visual interpretation of satellite imagery remains extremely demanding in terms of resources and time, especially when dealing with numerous multi-scale landslides affecting wide areas, such as is the case of rainfall-induced shallow landslides. Applying automated methods can contribute to more efficient landslide mapping and updating of existing inventories, and in recent years the number and variety of approaches is rapidly increasing (Holbling et al., 2012; Guzzetti et al., 2012; Marc and Hovius, 2015). Landslides can display highly heterogeneous sizes, which demands for information with higher spatial resolutions in the production of complete event inventories. Very High Resolution (VHR) panchromatic images, acquired by space-borne sensors with sub-metric precision, such as Ikonos, Quickbird, Geoeye and Worldview, are increasingly being considered as the best option for landslide mapping (van Westen et al., 2008), but these new levels of spatial detail also present new challenges to state of the art image analysis tools (Kurtz et al., 2014), asking for automated methods specifically suited to map landslide events on VHR optical images.

In recent years, several semi-automated methods were developed to tackle such difficulties, using specific classification schemes that target single post-event optical images (Cheng et al., 2013; Moosavi et al., 2014) or, when suitable pre-event data is available, exploit pre- and post-event image changes (e.g. Mondini et al., 2011a, b; Lu et al., 2011). In the latter case, great care has to be given to co-registration and radiometric correction procedures. Ideally, pre-event and post-event images should be acquired at the same time of the year, and with similar view angle and solar illumination, but such is usually not feasible (Guzzetti et al., 2012). The change detection approach can also be difficult to apply in very steep regions, because an accurate co-registration may not be possible (Chini et al., 2011; Pollard et al., 2010).

The various automated approaches recently developed for landslide mapping can also be grouped on the type of the image elements used, either "pixel based" (e.g., Chang et al., 2007; Cheng et al., 2013; Chini et al., 2011; Mondini et al., 2013, 2011a, b; Yang and Chen, 2010) or "object based" (e.g., Aksoy et al., 2012; Van Den Eeckhaut et al., 2012; Holbling et al., 2012; Lacroix et al., 2013; Lahousse et al., 2011; Lu et al., 2011; Martha et al., 2010, 2011, 2012, 2013; Stumpf et al., 2011). Especially for the improved resolution of VHR images, pixel-based methods are often less accurate than object oriented approaches, exhibiting a "salt and pepper" appearance (van Westen et al., 2008; Guzzetti et al., 2012). The "object oriented" approach, on the other hand, groups image pixels into homogeneous objects, which also contain shape, size, neighbouring, and textural features in addition to spectral information (Aksoy et al., 2012). In both cases, supervised and unsupervised classification schemes have been adopted, based on algorithms such as maximum likelihood (Borghuis et al., 2007; Danneels et al., 2007; Nichol et al., 2005), *k* nearest neighbour (Cheng et al., 2013; Li et al., 2013), Artificial Neural Network (Danneels et al., 2007; Nichol et al., 2005; Moosavi et al., 2014), Random Forest (Stumpf et al., 2011), or Support Vector Machine (Van Den Eeckhaut et al., 2012; Moosavi et al., 2014; Pisani et al., 2012).

The separation of the landslide affected region into source, transport and deposition areas is important to support post-event mitigation actions, since sediments deposited by landslides are likely to become source materials in subsequent events (Mondini et al., 2011a; Lira et al., 2013). More generally, the assessment of the volume of sediments produced, displaced and deposited by landslides is important for susceptibility and hazard evaluation (Guzzetti et al., 2009). Mondini et al. (2011a, 2013) developed automated pixel-based approaches to internally map landslides into source and run-out areas (defined as the union of transport and depositional areas), using a single post-event image, and pre- and post-event image changes, respectively.

In this work we develop and test a methodology for semi-automatic landslide recognition, and mapping of landslide source and run-out area. The method combines object-based image analysis and a Support Vector Machine supervised learning algorithm, and exploits information from VHR multispectral imagery acquired after a landslide event, together with a pre-event high resolution (4 m) LiDAR digital elevation model. We test the approach on a GeoEye-1 multispectral image (0.5 m panchromatic band), sensed 3 days after an exceptionally heavy rainfall episode in February 2010 that triggered thousands of shallow landslides and flash-floods across Madeira Island, in the North Atlantic, and claimed 45 lives (Lira et al., 2013). Section 2 describes the imagery and ancillary data used in the study, and the preparation of a landslide inventory to evaluate the results. In Sect. 3 we present our procedure for semi-automatic landslide mapping and the methodology for quality assessment. The results are presented in Sect. 4, followed by a brief discussion and conclusion in Sect. 5.

2 Data

2.1 Study area and imagery datasets

Madeira Island (Fig. 1) has a long record of flash floods, and since the beginning of the 19th century at least 30 flash flood events of significant intensity were registered (Baioni, 2011; Lira et al., 2013). These flash floods usually last a few hours during which a large amount of sediment is transported downstream, very quickly and with enormous energy. Large part of the transported material results from shallow landslides that are triggered upstream by the heavy precipitation (Lira et al., 2013). A combination of rough and steep terrain (mean slope angle 37 %) with intense rainfall provides the conditions for frequent and widespread landslides in Madeira.

On 20 February 2010 an extreme rainfall event followed a prolonged precipitation period (Luna et al., 2011; Fragoso et al., 2012; Couto et al., 2012; Teixeira et al., 2014). In the first few hours of that morning, rainfall values reached more than the double of the monthly average, triggering the landslides and the exceptionally strong flash floods that affected severely the municipalities of Funchal (home to half of the island population which totals 250 000) and Ribeira Brava (Lira et al., 2013).

Our study area (15 km^2-area rectangle in Fig. 1) covers one of the regions most affected by the 2010 landslide event in Madeira, in the south sector of the island, enclosing the main drainage basins upstream from the city of Funchal. Three days after the disaster, GeoEye-1 satellite was programmed, in the scope of GMES SAFER project, to acquire images over Madeira. The post-event GeoEye-1 image used in this analysis (Fig. 2) comprises 4 spectral bands (R, G, B and NIR) with 2.0 m pixel^{-1} resolution and one panchromatic band with 0.5 m pixel^{-1} resolution. In Fig. 2b one can observe the sediments transported downhill by the flood still flowing into the ocean in Funchal downtown area. Ancillary data used in this study includes orthophotomaps, with pre-event (2007) and post-event (2010) dates, and RGB bands with 0.4 m pixel^{-1} resolution; and a LIDAR pre-event DEM, with 4 m resolution. The LIDAR data were surveyed in 2009 with a Leica ALS50 airborne mapping system, with original point density 1 m^{-2}.

2.2 Landslide inventory

A landslide inventory dataset was prepared to train and evaluate the semi-automated method, by throughout revision of a previous inventory produced by Lira et al. (2013), based on delimitation of contours on the post-event GeoEye-1 image, and assisted by visual interpretation of orthophotomaps (acquired before and after the landslide event). Besides the revision of its contours, the landslides were classified according to the type of movement (Varnes, 1978; Cruden and Varnes, 1996; Zêzere, 2002), resorting to several data sources besides the imagery, namely field work reports and photographic evidence. The large majority of mass movements were shallow translational slides and debris flows. Debris flows are the fastest and most destructive type of landslide and important sources of sediment to channel networks; most begin as translational slides that liquefy (Sidle and Ochiai, 2006; Gabet and Mudd, 2006). For the drainage basins of the Funchal and Ribeira Brava municipalities, 3207 shallow translational slides and 795 debris flows were inventoried, besides 59 rotational slides. Furthermore, source and run-out areas were mapped separately inside the disturbed region, both for the shallow translational type of slides and debris flows. To distinguish between source and run-out areas was easier for fresh translational slides than for debris flows, but in both cases the process was affected by considerable uncertainty. We minimized the errors to some extent, by re-interpreting the same landslides on orthophotomaps acquired a couple of months later, when all loose material had been washed away from run-out areas. In some cases, source areas were divided into primary and secondary sources, the latter case corresponding to seemingly fresh slides occurring inside the run-out region.

3 Methods

The methodology followed is schematically represented in the diagram of Fig. 3. Pre-processing consisted first on fusing the 0.5 m resolution panchromatic band with the lower resolution R-G-B-NIR bands and orthorectifying the GeoEye-1 post-event image, using the orthophotomaps and the LIDAR DEM, as described in Lira et al. (2013). To ensure quality of pan-sharpening, the image bands were previously co-registered using 30–60 tie points, and interpolated and resampled with the nearest neighbour method. The pan sharpening band-fusion was performed with the Gram–Schmidt method available in ENVI software (Lira et al., 2013). Segmentation tests using co-registered stacks of the original bands were compared with segmentation using the pan-sharpened image and clearly indicated the superior performance of the last, as expected from previous studies findings (e.g. Sarkar and Kanungo, 2004). The study area (with 15 km^2, depicted in Figs. 1 and 5) was divided into a training area, from which the examples for learning were taken, and two smaller validation areas, which naturally did not contribute with examples for the training (see delimitation of training and validation areas in Fig. 5). Inventory data belonging to the training area was used to select optimal segmentation parameters. Following segmentation/merging steps to delineate the structures or objects available in the images, classification into landslide/non-landslide or source/non-source classes was performed through a set of describing features of spectral, textural and spatial natures.

3.1 Segmentation

The partition of the pansharpened and ortorectified GeoEye-1 image into objects was achieved with ENVI feature extraction module, which performs image segmentation followed by merging of the segmented regions. Image segmentation involved computation of a gradient image for each of the (R, G, B, NIR) fused bands using a Sobel edge detection operator (Sobel, 1968), followed by conversion to a single-band map, where each pixel retains the maximum gradient across the bands. A watershed algorithm (Beucher and Lantuéjoul, 1979; Roerdink and Meijster, 2001) is then applied, flooding the map starting with the lowest gradient values (the most uniform part of the objects) to the highest gradient values (the edges). A selectable scale parameter can modify the gradient map, hence controlling the minimum contrast of the object edges (ExelisVis, 2014; Jin, 2012; Roerdink and Meijster, 2001). A higher value of this parameter diminishes the local sensitivity which usually results in less and larger image objects. In the post-segmentation merging step, the spectral similarities of objects are evaluated and merged if their spectral properties are similar. To this effect, the mean spectral values for each band, in each adjacent object, and their Euclidean distance are computed, using the Full Lambda Schedule method (Robinson et al., 2002). A selectable merge parameter modifies the spectral distance threshold below which two adjacent objects can be merged, hence controlling the homogeneity of the pixels within the final segmented regions (ExelisVis, 2014).

Our goal in the segmentation/merging procedure was, first, to outline the landslides source and run-out areas, including the smallest of them, with as much accuracy as possible, and second, to avoid the division of these features into many objects, so as not to obscure its recognizable landslide shape. We tested several scale (5, 10, 20, 30, 40, 50, 60 and 70) and merge (30, 50, 70, 85, 90 and 95) parameters, and superposed the final segmented regions onto the landslide inventory (solely in the training area), to find the most appropriate combination to our case study (which turned out to be scale value 40, and merge value 90). Figure 4 shows details of the comparison between the inventory landslide delineation and our final choice for image partition.

3.2 Object features

From the 4 pan sharpened bands of GeoEye-1, a calculated vegetation index (NDVI), and 3 topographic indexes derived from a 4 m-resolution DTM (Table 1), a set of describing features of spectral, textural and spatial natures was computed for each object of the final partitioned image. In Table 1, "curvature profile" refers to the curvature of the surface in the direction of slope and "curvature plan" refers the curvature of the surface perpendicular to the slope direction.

The information from the 9 input layers in Table 1 was used to compute the full set of spectral, textural and spatial features available on ENVI feature extraction (as described in ExelisVis, 2014), resulting on 86 features for use in the object-based classification. We visually inspected the 86 color-coded object feature maps of the study area, and identified 75 maps as corresponding to features that can bring some actual knowledge into the classification. When later we compared training the SVM using either the selected group of features or the full set of features available, the results were very similar, which we interpreted as indicating low sensitivity of the algorithm to feature selection. Hence we chose to use currently all spectral, textural and spatial object features available, as shown in Table 2.

3.3 Supervised classification

Classification was based on the support vector machine (SVM) algorithm (Cortes and Vapnik, 1995), a supervised non-parametric statistical learning technique which separates the dataset into groups or classes in a way consistent with the training examples. SVMs are gaining increasing visibility in the remote sensing field due to their ability to successfully handle data with unknown statistical distributions and small training sets, as is often the case in remote sensing applications (Mountrakis et al., 2011). SVMs are binary classifiers whose aim is to find the decision region boundary that separates the dataset characteristics or features into two regions in the feature space. The SVM chooses the boundary (optimal hyper-plane) with the maximum safety margin to the closest training features (termed support vectors) hence maximizing the margin between the classes. The linearization of the decision boundary is achieved through the use of kernel functions which map the training data into a higher-dimensional space in which the two classes can be linearly separated by a hyper-plane.

As referred before, the study area (with 15 km^2, see Fig. 5) was divided into a training area, from which the examples for learning were taken, and two smaller validation areas. Care was taken to ensure that the validation areas contained regions characterized by diverse land cover and solar illumination. Example objects in the training set were retrieved from the reference inventory mapping, and represent a small percentage (1 %, about 1350 out of 130 400) of the total objects classified. Despite the larger dimensions of the training region, the number of landslides used as training examples was similar to the amount of landslides appearing in the validation areas. The choice of examples was expertise-driven, aiming at sampling the diverse characteristics of each class.

With the purpose to improve the performance of the SVM classification (Yang, 2011), we conducted several validation tests in order to choose the optimal SVM kernel function and corresponding parameters, namely the penalty parameter (that controls how examples located on the wrong side of the decision boundary are penalized), and the sigma function parameter. Within ENVI image processing environment, the SVM classifier was first tested on the training set described above using different kernel functions (linear, polynomial (degrees 2–6), sigmoid and radial basis function (RBF)) and ENVI's default SVM parameters. The RBF and degree 2 polynomial functions achieved the best prediction accuracy when checking with validation areas, and where used to further test, again by cross-validation between training and validation sets, the

Title Page
Abstract Introduction
Conclusions References
Tables Figures
◀| |▶
◀ ▶
Back Close
Full Screen / Esc
Printer-friendly Version
Interactive Discussion

penalty and sigma parameters. For both kernels, and ENVI's default penalty parameter (100), the SVM was tested for sigma values of 0.01, 0.02, 0.03, 0.04, 0.05, 0.06, 0.07, 0.08, 0.80, 0.1, 0.2, and 0.3. Furthermore, for the RBF kernel and for each sigma value of 0.03, 0.04 and 0.2, the SVM was tested for penalty values of 1, 10, 50, 75, 100, 125, 150, 200, 250, 300, 350, 400, 450, 500, 750, and 1000. Finally, for the degree 2 polynomial kernel, and for each sigma value of 0.03 and 0.04, the SVM was tested for penalty values of 100, 125, 150, 200, and 250. We finally choose the RBF kernel with sigma value 0.03 and penalty parameter 200 for achieving the best prediction accuracy. The classification confidence threshold was set to 90 %, and objects whit less than 90 % confidences in each class were set to unclassified.

To address our multiclass classification problem (landslide source; landslide run-out; all others) we started by using two "one-against-all approaches", in which a landslide-against-all and a source-against-all classifiers were designed to derive the classes "landslide", "landslide source" and "all others"; subsequently, the class "landslide run-out" was obtained from spatial subtraction of classes "landslide" and "landslide source". The feature information used by the SVM classifier was described in Sect. 3.2 and is listed in Tables 1 and 2. The features associated with landslide/non-landslide examples or source/non-source examples are plotted by the algorithm into its corresponding feature spaces for definition of the decision boundaries. Then the entire image is classified: for each one-against-all approach, and for each object on the image, the SVM maps its spectral, spatial and textural characteristics into the feature space and, depending on which side of the decision boundary it locates, classifies it accordingly.

3.4 Accuracy assessment

For assessment of the accuracy of the classified image we compared the results in the validations areas with the landslide inventory map (Lahousse et al., 2001; Holbling et al., 2012), and followed standard metrics derived from the error or confusion matrix built from the two data sets (Congalton, 1991; Foody, 2002). The accuracy metrics computed were: the overall accuracy (acc), which gives the proportion of area correctly classified, expressed as a percentage; the kappa index of agreement (k), a measure of reliability which gives the proportion of agreement corrected for chance between two cases; and the omission (false negatives) and commission (false positive) errors.

4 Results

Following the methodology already described, landslide classification maps were produced for the 15 km^2-wide study area located within one of the regions most affected by the 2010 landslide event in Madeira. Generally speaking, our approach has proved successful in the recognition of landslides and internal mapping of its source areas. In this section we present, evaluate, and discuss the results, which are divided into two parts: (i) landslide recognition and delineation and (ii) internal mapping of source and run-out areas.

4.1 Landslide recognition

Figure 5 presents, for the overall study area, the object-based image classification of landslides, using the SVM machine learning algorithm with the RBF kernel, as described before. To illustrate the performance of the approach, the automatically recognized landslides are compared to the inventory reference data (yellow fill and red contours in Fig. 5, respectively). We observe a remarkable accurate automated depiction of the landslide areas, both in the training region or in the validation regions. Landslides not successfully detected are located in areas obscured by shadows, an unavoidable hindrance in this approach.

In Fig. 6 the detailed mapping of the landslide areas is presented for the validation regions 1 and 2, which did not contribute with examples for learning. The figure also summarizes the accuracy metrics computed from the error matrix built for each of the validation areas, yielding good results for both of them, with commission errors below 26 % and omission errors below 24 %.

Validation area 2, which contains a poorly illuminated slope, displays somewhat poorer accuracy in the classification of the overall area affected by land sliding. However, this problem is overcome by the source-against-all classification results (next Sect. 4.2), which performed well in what concerns landslide recognition: 61 out of 63 landslides were detected in this region, which compares with 20 out of 22 landslides in validation region 1 (see Fig. 7a and b). These values correspond to the detection of 95 % of the landslides scars in the validation areas.

4.2 Separation of source and run-out areas

Figure 7 displays the results of the automated mapping of landslide source and landslide run-out (transport plus deposition) in the validation areas 1 and 2, using again the object-based and SVM machine learning approaches described in Sect. 3.

In Fig. 8 a detail of the classification is shown to allow comparison with the landslide characteristics that can be visually recognized in the pan sharpened GeoEye image.

The inspection of Figs. 7 and 8 shows an essentially good performance of the classifier in the internal mapping of source and run-out landslide areas, in particular in the sunnier east-facing slopes. In the less illuminated areas the classifier is able to accurately map the source areas, but performs poorly in what concerns the landslide run-out mapping (Fig. 7). Accuracy measures were again computed for each of the validation areas, by comparison with source and run-out areas in reference data. Two cases need to be distinguished, depending if reference data source areas are defined as primary sources (example in Fig. 7b) or also include secondary sources, which we defined as seemingly fresh slides occurring inside the run-out region (Figs. 7a and 8).

Table 3 lists the computed overall accuracies, kappa indexes and false negative/positive rates (FNR/FPR) for both validation areas, and for both definitions of source area. False negative and false positive rates fall below 38 and 78 %, respectively, for all situations (the results in Fig. 7 correspond to the best cases). The overall precision seems hindered, in one hand, by the difficulties of the classifier in mapping the run-outs in poorly illuminated areas, and on the other hand, by the subjectivity of reference data definition of primary and secondary sources of sediment.

5 Conclusions

We presented a method for semi-automatic landslide recognition, and mapping of landslide source and run-out area, suitable for VHR remote sensing images of rain-induced landslide events. The approach combines object-based image analysis and a Support Vector Machine supervised learning algorithm, which was tested with a GeoEye-1 multispectral image (0.5 m panchromatic band), sensed 3 days after widespread landslides and flash-floods in Madeira Island, using as ancillary data a pre-event high resolution (4 m) LiDAR digital elevation model. Our study confirms the high suitability of VHR multispectral images for landslide mapping (van Westen et al., 2008), in particular by automated methods, expanding the number of automatic applications that target single post-event optical images (e.g. Cheng et al., 2013; Moosavi et al., 2014), a choice less demanding in terms of pre-processing than the change detection approaches more usually found in the literature (e.g. Mondini et al., 2011a, b; Lu et al., 2011), for which it is especially important to pay attention to co-registration and radiometric correction (Guzzetti et al., 2012). Our results also broadens the growing number of applications of object-based image analysis (OBIA) for automated landslide mapping, providing insight into the advantage of using also spatial and textural features in the classification, and not only spectral attributes as in the pixel-based approach. Very few previous landslide studies have integrated OBIA and Support Vector Machines (Moosavi et al., 2014) and we confirm it as a robust and efficient approach, being able to detect 95 % of the number of landslides scars present in the validation areas. Also, to our knowledge, no previous studies have used OBIA to tackle the problem of automated mapping of landslide source and run-out area. Mondini et al. (2011a, 2013) developed automated pixel-based approaches to deal with this issue, and our OBIA results compare well with theirs.

At present, one of the main limitations of the methodology proposed is the poor performance obtained in the automatic mapping of landslide transport and deposition areas in poorly illuminated slopes, a problem that may perhaps only be overcome using multiple satellite acquisition geometries. Another source of uncertainty results from the subjectivity associated with the definition of the landslide source areas, made mostly from visual inspection of post-event satellite images and orthophotomaps. These difficulties may have constrained the quantitative assessment of the classifier results. This task was particularly challenging in the case of debris flows, in which the high-energy transport area seemed to contain secondary sources of sediment supply (see examples in Fig. 8), with the same spectral and textural image characteristics of the primary sources.

The method proposed here has the potential to increase promptness and cost-effectiveness in the production of inventories following a landslide event, when a VHR post-event optical image and a pre-event DEM are available. It also assists an approximate spatial quantification of the amount of sediments produced and transported during a landslide event, an information that can be crucial in emergency response situations, and is definitely important for landslide susceptibility and hazard assessment (Guzzetti et al., 2009), contributing in particular to support post-event mitigation actions, such as sediment control measures (Lira et al., 2013).

References

Aksoy, B. and Ercanoglu, M.: Landslide identification and classification by object-based image analysis and fuzzy logic: an example from the Azdavay region (Kastamonu,Turkey), Comput. Geosci., 38, 87–98, 2012.

Baioni, D.: Human activity and damaging landslides and floods on Madeira Island, Nat. Hazards Earth Syst. Sci., 11, 3035–3046, doi:10.5194/nhess-11-3035-2011, 2011.

Barlow, J., Franklin, S., and Martin, Y.: High spatial resolution satellite imagery, DEM derivatives, and image segmentation for the detection of mass wasting processes, Photogramm. Eng. Rem. S., 72, 687–692, 2006.

Beucher, S. and Lantuejoul, C.: Use of watersheds in contour detection, in: Proceedings International Workshop on Image Processing, Real-Time Edge and Motion Detection/Estimation, Rennes, France, 17–21 September 1979, 2.1–2.12, 1979.

Borghuis, A. M., Chang, K., and Lee, H. Y.: Comparison between automated and manual mapping of typhoon-triggered landslides from SPOT-5 imagery, Int. J. Remote Sens., 28, 1843–1856, 2007.

Bucknam, R. C., Coe, J. A., Chavarría, M. M., Godt, J. W., Tarr, A. C., Bradley, L.-A., Rafferty, S., Hancock, D., Dart, R. L., and Johnson, M. L.: Landslides Triggered by Hurricane Mitch in Guatemala – Inventory and Discussion, USGS, Denver, Colorado, Open-File Report, 443 pp., 2001.

Chang, Y.-L., Liang, L.-S., Han, C.-C., Fang, J.-P., Liang, W.-Y., and Chen, K.-S.: Multisource data fusion for landslide classification using generalized positive Boolean functions, IEEE T. Geosci. Remote, 45, 1697–1708, doi:10.1109/TGRS.2007.895832, 2007.

Cheng, G., Guo, L., Zhao, T., Han, J., Li, H., and Fang, J.: Automatic landslide detection from remote-sensing imagery using a scene classification method based on BoVW and pLSA, Int. J. Remote Sens., 34, 45–59, 2013.

Chini, M., Cinti, F. R., and Stramondo, S.: Co-seismic surface effects from very high resolution panchromatic images: the case of the 2005 Kashmir (Pakistan) earthquake, Nat. Hazards Earth Syst. Sci., 11, 931–943, doi:10.5194/nhess-11-931-2011, 2011.

Congalton, R. G.: A review of assessing the accuracy of classifications of remotely sensed data, Remote Sens. Environ., 37, 35–46, 1991.

Cortes, C. and Vapnik, V.: Support-vector networks, Mach. Learn., 20, 273–297, 1995.

Couto, F. T., Salgado, R., and Costa, M. J.: Analysis of intense rainfall events on Madeira Island during the 2009/2010 winter, Nat. Hazards Earth Syst. Sci., 12, 2225–2240, doi:10.5194/nhess-12-2225-2012, 2012.

Cruden, D. M. and Varnes, D. J.: Landslide types and processes, in: Landslides, Investigation and Mitigation, Transportation Research Board, edited by: Turner, A. K. and Shuster, R. L., Special Report 247, National Academy Press, Washington DC, 36–75, 1996.

Danneels, G., Pirard, E., and Havenith, H. B.: Automatic landslide detection from remote sensing images using supervised classification methods, in: Proceedings of IGARSS 2007 – IEEE International Geoscience and Remote Sensing Symposium, 23–28 July 2007, Barcelona, 3014–3017, 2007.

ExelisVis: available at: http://www.exelisvis.com/docs/BackgroundSegmentationAlgorithm.html, http://www.exelisvis.com/docs/BackgroundMergeAlgorithms.html, www.exelisvis.com/docs/Example_Based_Classification.html,last access: 16 September 2015, 2015.

Fragoso, M., Trigo, R. M., Pinto, J. G., Lopes, S., Lopes, A., Ulbrich, S., and Magro, C.: The 20 February 2010 Madeira flash-floods: synoptic analysis and extreme rainfall assessment, Nat. Hazards Earth Syst. Sci., 12, 715–730, doi:10.5194/nhess-12-715-2012, 2012.

Foody, G. M.: Status of land cover classification accuracy assessment, Remote Sens. Environ., 80, 185–201, 2002.

Gabet, E. and Mudd, S.: The mobilization of debris flows from shallow landslides, Geomorphology, 74, 207–218, 2006.

Guzzetti, F., Ardizzone, F., Cardinali, M., Rossi, M., and Valigi, D.: Landslide volumes and landslide mobilization rates in Umbria, central Italy, Earth Planet. Sc. Lett., 279, 222–229, 2009.

Guzzetti, F., Mondini, A., Cardinali, M., Fiorucci, F., Santangelo, M., and Chang, K.: Landslide inventory maps: new tools for an old problem, Earth-Sci. Rev., 112, 42–66, 2012.

Heleno, S., Matias, M., Vasconcelos, M., Sousa, J., and Pina, P.: Automated OBIA mapping and classification of rain-induced landslides with VHR post-event optical images and HR pre-event LiDAR DEM, South-Eastern European Journal of Earth Observation and Geomatics, 3, 271–274, 2014.

Holbling, D., Füreder, P., Antolini, F., Cigna, F., Casagli, N., and Lang, S.: A semi-automated object-based approach for landslide detection validated by persistent scatterer interferometry measures and landslide inventories, Remote Sensing, 4, 1310–1336, 2012.

Jin, X.: Segmentation-Based Image Processing System, US Patent 8,260,048, filed 14 November 2007, issued 4 September 2012.

Joyce, K. E.,Dellow, G. D., and Glassey, P. J.: Assessing image processing techniques for mapping landslides, in: Proceedings of IGARSS 2008 – IEEE International Geoscience and Remote Sensing Symposium, 7–11 July 2008, Boston, MA, 1231–1234, 2008.

Kurtz, C., Stumpf, A., Malet, J., Gançarski, P., Puissant, A., and Passat, N.: Hierarchical extraction of landslides from multiresolution remotely sensed optical images, ISPRS J. Photogramm., 87, 122–136, 2014.

Lacroix, P., Zavala, B., Berthier, E., and Audin, L.: Supervised method of landslide inventory using panchromatic SPOT5 images and application to the earthquake-triggered landslides of Pisco (Peru, 2007, Mw8.0), Remote Sensing, 5, 2590–2616, 2013.

Lahousse, T., Chang, K. T., and Lin, Y. H.: Landslide mapping with multi-scale object-based image analysis – a case study in the Baichi watershed, Taiwan, Nat. Hazards Earth Syst. Sci., 11, 2715–2726, doi:10.5194/nhess-11-2715-2011, 2011.

Li, Y., Chen, G., Wang, B., Zheng, L., Zhang, Y., and Tang, C.: A new approach of combining aerial photography with satellite imagery for landslide detection, Nat. Hazards, 66, 649–669, 2013.

Lira, C., Lousada, M., Falcão, A. P., Gonçalves, A. B., Heleno, S., Matias, M., Pereira, M. J., Pina, P., Sousa, A. J., Oliveira, R., and Almeida, A. B.: The 20 February 2010 Madeira Island flash-floods: VHR satellite imagery processing in support of landslide inventory and sediment budget assessment, Nat. Hazards Earth Syst. Sci., 13, 709–719, doi:10.5194/nhess-13-709-2013, 2013.

Lu, P., Stumpf, A., Kerle, N., and Casagli, N.: Object-oriented change detection for landslide rapid mapping, IEEE Geosci. Remote S., 8, 701–705, 2011.

Luna, T., Rocha, A., Carvalho, A. C., Ferreira, J. A., and Sousa, J.: Modelling the extreme precipitation event over Madeira Island on 20 February 2010, Nat. Hazards Earth Syst. Sci., 11, 2437–2452, doi:10.5194/nhess-11-2437-2011, 2011.

Malamud, B. D., Turcotte, D. L., Guzzetti, F., and Reichenbach, P.: Landslide inventories and their statistical properties, Earth Surf. Proc. Land., 29, 687–711, 2004.

Marc, O. and Hovius, N.: Amalgamation in landslide maps: effects and automatic detection, Nat. Hazards Earth Syst. Sci., 15, 723–733, doi:10.5194/nhess-15-723-2015, 2015.

Martha, T. R. and Kumar, K. V.: September 2012 landslide events in Okhimath, India – an assessment of landslide consequences using very high resolution satellite data, Landslides, 10, 469–479, 2013.

Martha, T. R., Kerle, N., Jetten, V., van Westen, C. J., and Kumar, K. V.: Characterising spectral, spatial and morphometric properties of landslides for semi-automatic detection using object-oriented methods, Geomorphology, 116, 24–36, 2010.

Martha, T. R., Kerle, N., van Westen, C. J., Jetten, V., and Kumar, K. V.: Segment optimization and data-driven thresholding for knowledge-based landslide detection by object-based image analysis, IEEE T. Geosci. Remote, 49, 4928–4943, 2011.

Martha, T. R., Kerle, N., van Westen, C. J., Jetten, V., and Kumar, K. V.: Object-oriented analysis of multi-temporal panchromatic images for creation of historical landslide inventories, ISPRS J. Photogramm., 67, 105–119, 2012.

Mondini, A., Chang, K., and Yin, H.: Combining multiple change detection indices for mapping landslides triggered by typhoons, Geomorphology, 134, 440–451, 2011a.

Mondini, A., Guzzetti, F., Reichenbach, P., Rossi, M., Cardinali, M., and Ardizzone, F.: Semi-automatic recognition and mapping of rainfall induced shallow landslides using optical satellite images, Remote Sens. Environ., 115, 1743–1757, 2011b.

Mondini, A. C., Marchesini, I., Rossi, M., Chang, K.-T., Pasquariello, G., and Guzzetti, F.: Bayesian framework for mapping and classifying shallow landslides exploiting remote sensing and topographic data, Geomorphology, 201, 135–147, 2013.

Mondini, A. C., Viero, A., Cavalli, M., Marchi, L., Herrera, G., and Guzzetti, F.: Comparison of event landslide inventories: the Pogliaschina catchment test case, Italy, Nat. Hazards Earth Syst. Sci., 14, 1749–1759, doi:10.5194/nhess-14-1749-2014, 2014.

Moosavi, V., Talebi, A., and Shirmohammadi, B.: Producing a landslide inventory map using pixel-based and object-oriented approaches optimized by Taguchi method, Geomorphology, 204, 646–656, 2014.

Mountrakis, G., Im, J., and Ogole, C.: Support vector machines in remote sensing: a review, ISPRS J. Photogramm., 66, 247–259, 2011.

Nichol, J. and Wong, M. S.: Satellite remote sensing for detailed landslide inventories using change detection and image fusion, Int. J. Remote Sens., 26, 1913–1926, 2005.

Pisani, R., Riedel, P., Costa, K., Nakamura, R., Pereira, C., Rosa, G., and Papa, J.: Automatic landslide recognition through optimum-path forest, in: Proceedings of IGARSS 2012 – IEEE International Geoscience and Remote Sensing Symposium, 22–27 July 2012, Munich, 6228–6231, 2012.

Pollard, T. B., Eden, I., Mundy, J. L., and Cooper, D. B.: A volumetric approach to change detection in satellite images, Photogramm. Eng. Rem. S., 76, 817–831, 2010.

Robinson, D. J., Redding, N. J., and Crisp, D. J.: Implementation of a Fast Algorithm For Segmenting SAR Imagery, Scientific and Technical Report, Defense Science and Technology Organization, Australia, 2002.

Roerdink, J. B. T. M. and Meijster, A.: The watershed transform: definitions, algorithms, and parallelization strategies, Fund. Inform., 41, 187–228, 2001.

Sarkar, S. and Kanungo, D. P.: An integrated approach for landslide susceptibility mapping using remote sensing and GIS, Photogramm. Eng. Rem. S., 70, 617–625, 2004.

Sidle, R. C. and Ochiai, H.: Landslides: processes, prediction, and land use, in: Water Resources Monograph, 18, American Geophysical Union, Washington, DC, 1–312, 2006.

Sobel, I.: An isotropic 3 × 3 image gradient operator, Presentation at Stanford Artificial Intelligence Project (SAIL), Stanford, California, doi:10.13140/RG.2.1.1912.4965, 1968.

Stumpf, A. and Kerle, N.: Object-oriented mapping of landslides using Random Forests, Remote Sens. Environ., 115, 2564–2577, 2011.

Teixeira, J. C., Carvalho, A. C., Carvalho, M. J., Luna, T., and Rocha, A.: Sensitivity of the WRF model to the lower boundary in an extreme precipitation event – Madeira island case study, Nat. Hazards Earth Syst. Sci., 14, 2009–2025, doi:10.5194/nhess-14-2009-2014, 2014.

Van Den Eeckhaut, M. V. D., Kerle, N., Poesen, J., and Hervás, J.: Object-oriented identification of forested landslides with derivatives of single pulse LiDAR data, Geomorphology, 173–174, 30–42, 2012.

Van Westen, C. J., van Asch, T. W. J., and Soeters, R.: Landslide hazard and risk zonation - why is it still so difficult?, B. Eng. Geol. Environ., 65, 167–184, 2006.

Van Westen, C. J., Castellanos, E., and Kuriakose, S. L.: Spatial data for landslide susceptibility, hazard, and vulnerability assessment: an overview, Eng. Geol., 102, 112–131, 2008.

Varnes, D. J.: Slope movement types and processes, in: Landslides – Analysis and Control, edited by: Schuster, R. L. and Krizek, R. J., Special Report 176, Transportation Research Board, National Academy of Science, Washington DC, 11–33, 1978.

Xu, C., Xu, X., Bruce, J., and Shyu, H.: Database and spatial distribution of landslides triggered by the Lushan, China Mw 6.6 earthquake of 20 April 2013, Geomorphology, 248, 77–92, doi:10.1016/j.geomorph.2015.07.002, 2015.

Yang, X.: Parameterizing support vector machines for land cover classification, Photogramm. Eng. Rem. S., 77, 27–37, 2011.

Yang, X. and Chen, L.: Using multi-temporal remote sensor imagery to detect earthquake-triggered landslides, Int. J. Appl. Earth Obs., 12, 487–495, 2010.

Zêzere, J. L.: Landslide susceptibility assessment considering landslide typology. A case study in the area north of Lisbon (Portugal), Nat. Hazards Earth Syst. Sci., 2, 73–82, doi:10.5194/nhess-2-73-2002, 2002.

Table 1. Layers used in classification.

Spectral bands	Vegetation index	Topographic index
RED (50 cm) GREEN (50 cm) BLUE (50 cm) NIR (50 cm)	NDVI (50 cm)	Slope (4 m) Aspect (4 m) Curvature profile (4 m) Curvature plan (4 m)

Title Page
Abstract Introduction
Conclusions References
Tables Figures
◀| |▶
◀ ▶
Back Close
Full Screen / Esc
Printer-friendly Version
Interactive Discussion

Table 2. Features used for object-based learning.

Categories	Features	
Spectral features	– Mean – Standard deviation – Maximum – Minimum	The spectral mean, SD, max and min value of the pixels inside the segmented region are computed for each spectral band, vegetation and topographic indexes.
Texture features	– Range – Variance – Entropy	A 3 × 3 moving window computes range, variance and entropy of the pixels inside it, followed by averaging inside the segmented region.
Spatial features	– Area – Length – Compacteness – Roundness – Form factor – Convexity	– Elongation – Major length – Minor length – Rectangular fit – Main direction – Number of holes

Table 3. Accuracy measures for classification of landslide source and run-out, for different validation areas and source definitions.

	Primary sources				Primary and secondary sources			
	acc	*k*	FNR	FPR	acc	*k*	FNR	FPR
VAL 1	98.4	0.34	24.9	77.2	98.4	0.48	36.7	60.3
VAL 2	97.6	0.48	18.9	64.7	97.4	0.58	37.5	44.1

acc: overall accuracy (%); *k*: Kappa index; FNR: False Negative Rate (%); FNP: False Positive Rate (%).

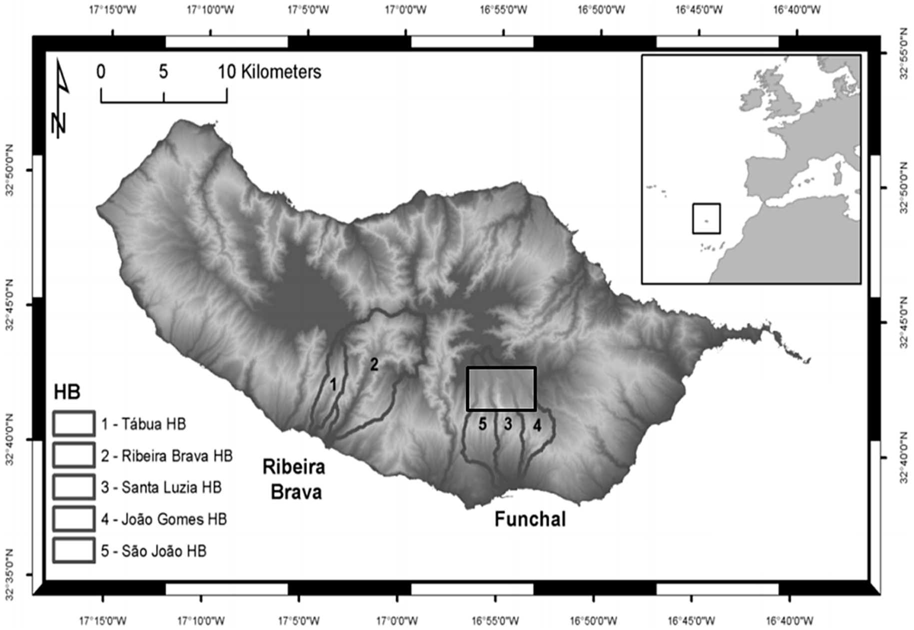

Figure 1. Location of Madeira Island, in the North Atlantic, with the most affected basins during the 2010 event superimposed on a DTM. Our study area is delimited by the rectangle located over Funchal basins. Adapted from Lira et al. (2013).

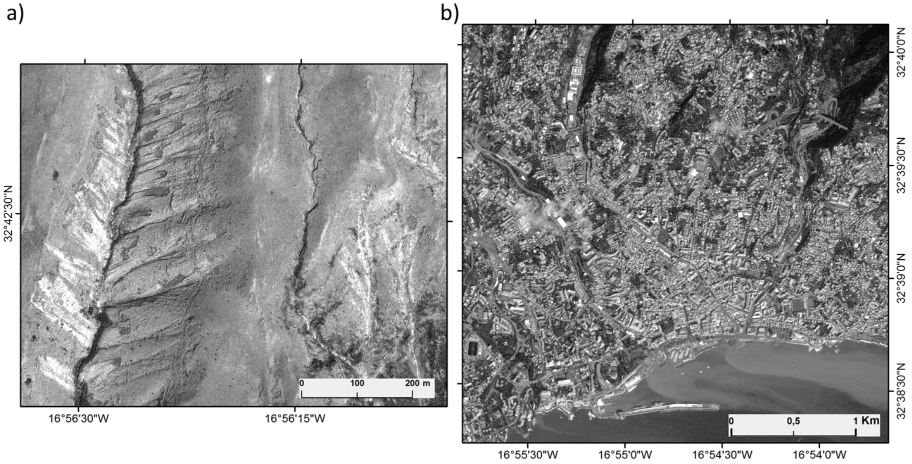

Figure 2. Details of Geoeye-1 pan-sharpened RGB image, shown in grayscale, acquired over Madeira three days after the flash-floods.

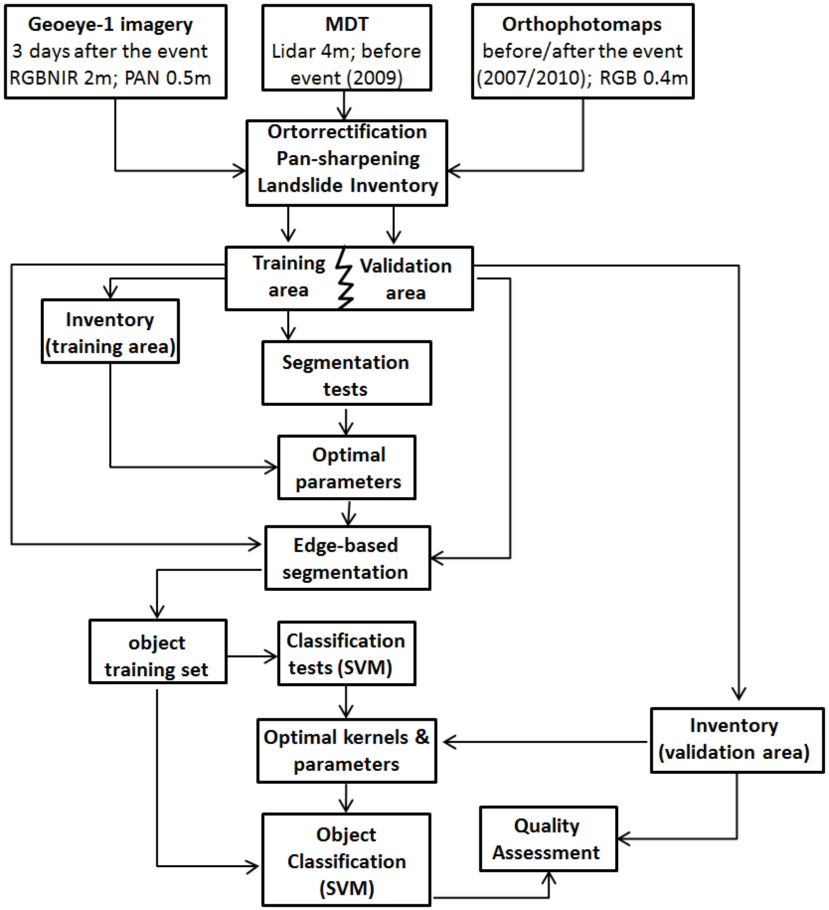

Figure 3. Diagram of the landslide mapping methodology.

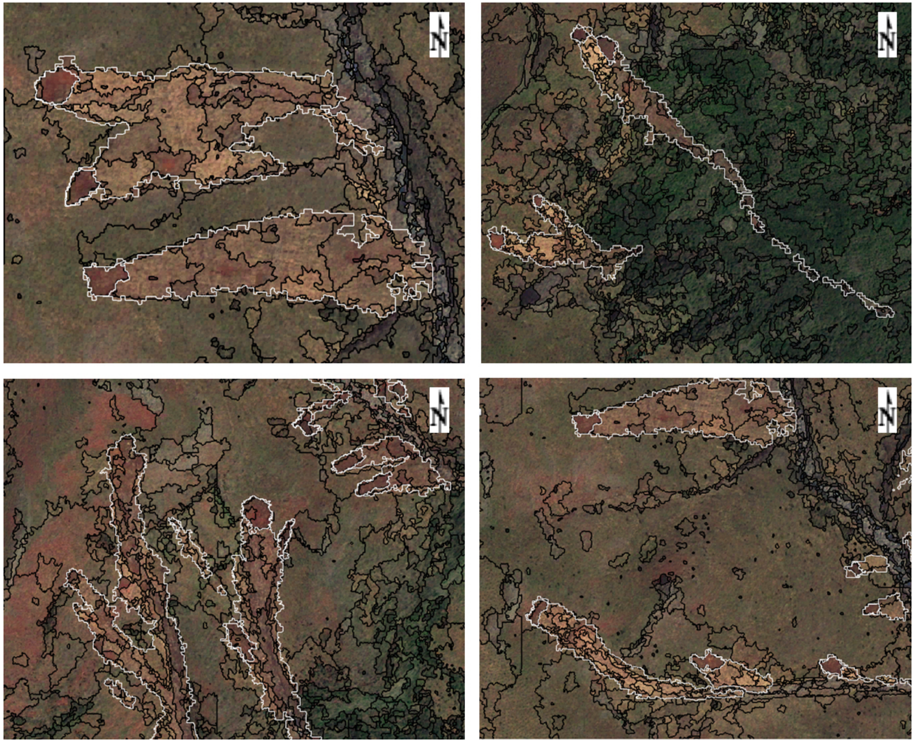

Figure 4. Details of Geoeye-1 pan-sharpened RGB image, showing the chosen segmentation/merging parameters: scale 40, merge 90; white contour – inventory landslide delineation; black contour – image partition.

Title Page
Abstract | Introduction
Conclusions | References
Tables | Figures
◀| |▶
◀ ▶
Back | Close
Full Screen / Esc
Printer-friendly Version
Interactive Discussion

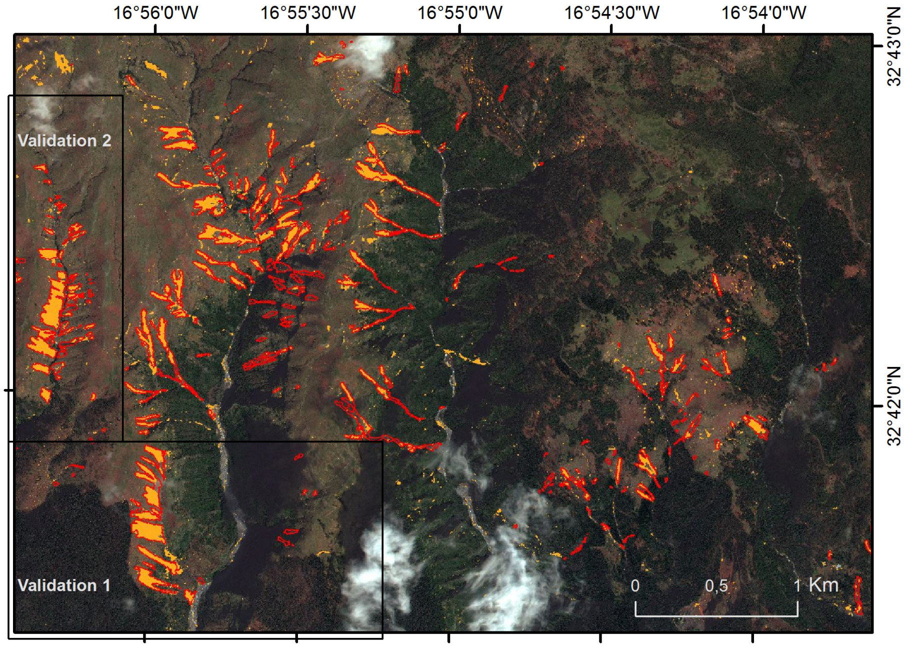

Figure 5. Geoeye-1 pan-sharpened RGB image over the study area (15Km2) showing the results of object-based SVM (RBF) landslide mapping. The area automatically classified as landslide (yellow fill) is compared to inventory reference data (red contours). Outlines of validation areas 1 and 2 also shown.

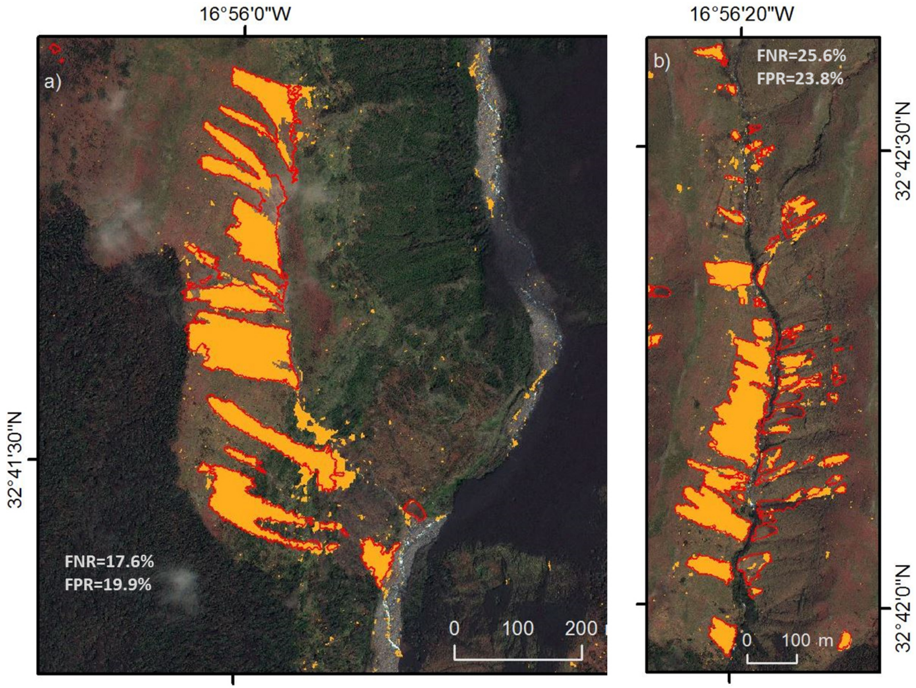

Figure 6. Details of previous figure, showing classified landslides (yellow fill) compared to inventory reference data (red contours) in the validation regions 1 **(a)** and 2 **(b)**.

NHESSD

3, 5633–5664, 2015

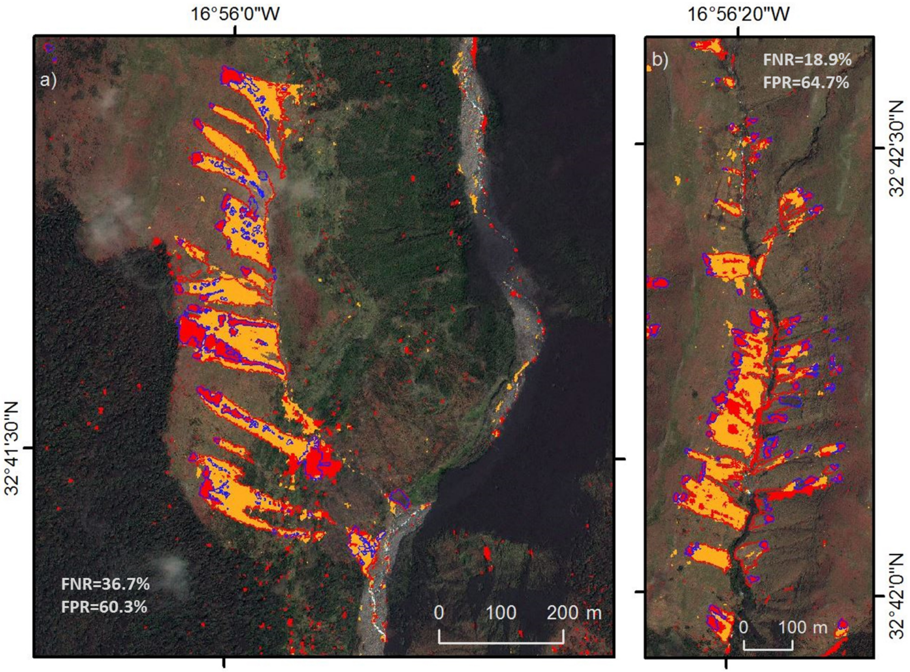

Figure 7. Classified landslide sources (red fill) and run-out (yellow fill) compared to inventory reference data (red contours delineate the landslide; blue contours delineate the source area). In the examples shown, source areas are defined either as primary sources (in **b**, validation region 2) or also including secondary sources of sediment (in **a**, validation region 1). Geoeye-1 pan-sharpened RGB composite as base image.

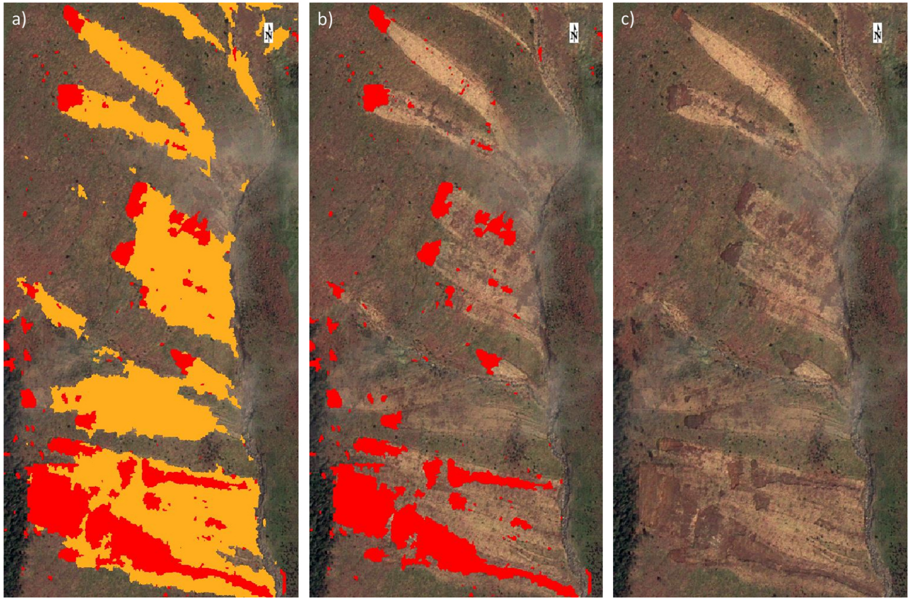

Figure 8. Detail of classification of landslide sources (red fill, **a** and **b**) and run-out (yellow fill, in **a** compared with base image **c**). Geoeye-1 pan-sharpened RGB composite as base image.